



# Significant spatial patterns from the GCM seasonal forecasts of global precipitation

Tongtiegang Zhao<sup>1</sup>, Wei Zhang<sup>2</sup>, Yongyong Zhang<sup>3</sup>, and Xiaohong Chen<sup>1</sup>

<sup>1</sup>Center of Water Resources and Environment, Sun Yat-Sen University, Guangzhou 510275, China

5 <sup>2</sup>IIHR-Hydroscience & Engineering, University of Iowa, Iowa City 52242, United States

<sup>3</sup>Key Laboratory of Water Cycle and Related Land Surface Processes, Chinese Academy of Sciences, Beijing 100101, China

Correspondence to: Tongtiegang Zhao ([zhaottg@mail.sysu.edu.cn](mailto:zhaottg@mail.sysu.edu.cn))

**Abstract:** Fully-coupled global climate models (GCMs) generate a vast amount of high-dimensional forecast data of the global climate; therefore, interpreting and understanding the predictive performance is a critical issue in applying GCM forecasts. Spatial plotting is a powerful tool to identify where forecasts perform well and where forecasts are not satisfactory. Here we build upon the spatial plotting of anomaly correlation between forecast ensemble mean and observations and derive significant spatial patterns to illustrate the predictive performance. For the anomaly correlation derived from the ten sets of forecasts archived in the North America Multi-Model Ensemble (NMME) experiment, the global and local Moran's I are calculated to associate anomaly correlation at neighbouring grid cells to one another. The global Moran's I indicates that at the global scale anomaly correlation at one grid cell relates significantly and positively to anomaly correlation at surrounding grid cells, while the local Moran's I reveals clusters of grid cells with high, neutral, and low anomaly correlation. Overall, the forecasts produced by GCMs of similar settings and at the same climate center exhibit similar clustering of anomaly correlation. In the meantime, the forecasts in NMME show complementary performances. About 80% of grid cells across the globe fall into the cluster of high anomaly correlation under at least one of the ten sets of forecasts. While anomaly correlation exhibits substantial spatial variability, the clustering approach serves as a filter of noise to identify spatial patterns and yields insights into the predictive performance of GCM seasonal forecasts of global precipitation.

## 1 Introduction

Global climate models (GCMs) have been steadily improved over the past decades and are being employed by major climate centers around the world to generate operational long-range forecasts [Doblas-Reyes et al., 2013; Saha et al., 2014; Bauer et al., 2015; Hudson et al., 2017; Kushnir et al., 2019], providing physically-based forecasts in comparison to conventional statistical forecasts [Mason and Goddard, 2001; Wu et al., 2009; Schepen et al., 2012]. In particular, the fully-coupled GCMs assimilate world-wide observational information to predict the global hydrological cycle [Merryfield et al., 2013; Saha et al., 2014; Jia et al., 2015]. Equipped with physical and dynamical laws, GCMs can potentially make forecasts of longer lead time and higher skill than statistical models [Kirtman et al., 2014; Becker et al., 2014; Chen et al., 2017]. In terms of computation, global climate forecasting is as complex as the simulation of the human brain and of the evolution of the early



Universe [Bauer et al., 2015]. Advances in super-computing facilitate the forecasting and make GCM forecasts readily available for hydrological, environmental, and agricultural modelling [Sheffield et al., 2014; Vecchi et al., 2014; Bellprat et al., 2019; Pappenberger et al., 2019; Zhao et al., 2019].

GCMs generate a vast amount of high-dimensional forecast data, including retrospective forecasts of past climate and real-time forecasts [Kirtman et al., 2014; Saha et al., 2014; Jia et al., 2015]. Due to the complexity of atmospheric processes and model physics, the predictive performance of GCM forecasts is not uniform but varies considerably across the globe [Yuan et al., 2013; Tian et al., 2017; Zhao et al., 2018]. Therefore, interpreting and understanding the predictive performance is a critical issue in the applications of GCM forecasts [Doblas-Reyes et al., 2013; Merryfield et al., 2013; Saha et al., 2014; Jia et al., 2015; Hudson et al., 2017]. There are various metrics to verify the attributes of forecasts [Murphy, 1993]. For example, bias in percentage indicates the extent to which the forecasts are persistently higher, or lower, than the corresponding observations; probability integral transform (PIT) evaluates the reliability of the spread of ensemble GCM forecasts in capturing the distribution of observations; and the continuous ranked probability score (CRPS) is a probability-weighted measure of the errors of ensemble members in relation to the observations [Murphy, 1993; Hersbach, 2000; Gneiting et al., 2007]. The anomaly correlation that indicates how well large (small) values of forecasts correspond to large (small) values of observations is one of the most popular metrics [e.g., Yuan et al., 2011; Saha et al., 2014; Crochemore et al., 2016; Hudson et al., 2017; Zhao et al., 2017]. Compared to PIT that requires a diagnostic plot and CRPS that relies on numerical integration, anomaly correlation is conceptually simple, easy to implement, and also robust to missing and censored values [Yuan et al., 2011; Luo et al., 2014; Slater et al., 2017].

Spatial plotting with latitude and longitude has been extensively used to handle the dimensionality for the verification of GCM forecasts [Kirtman et al., 2014; Hudson et al., 2017; Slater et al., 2017]. The fact that forecasts are commonly generated by GCMs as grid-based data makes spatial plotting a particular tool of choice for verification [Merryfield et al., 2013; Saha et al., 2014; Jia et al., 2015]. As to anomaly correlation, spatial plotting overcomes tedious eyeball search by grid cell and is effective in locating where there is a good correspondence between forecasts and observations and where the correspondence is not satisfactory [Yuan et al., 2011; Luo et al., 2013; Saha et al., 2014; Sheffield et al., 2014; Crochemore et al., 2016]. Similarly, spatial plotting applies to other verification metrics, such as bias and CRPS, and facilitates the examination of forecast attributes [Hersbach, 2000; Gneiting et al., 2007; Kirtman et al., 2014].

The extensive use of spatial plotting underlines the importance of testing the significance of spatial patterns. In spatial statistics, one of the fundamental issues is “are the spatial patterns displayed by the spatial plots significant in some sense and therefore worth interpreting?” [Cliff and Ord, 1981; Anselin, 1995; Getis, 2007]. However, the test of significance is commonly missing in the spatial plotting of GCM forecasts. In other words, verification metrics, such as anomaly correlation, are calculated for each grid cell and then shown as they are. To some extent, the interpretation of predictive performance depends on the color schemes, which are selected subjectively to represent the scale of verification metrics. There is the first law of geography – “everything is related to everything else, but near things are more related than distant things” [Tobler, 1970]. As to spatial plotting, the indication is that when verifying forecasts at one grid cell, attention also needs to be paid to



65 forecasts at surrounding grid cells. For anomaly correlation, a grid cell with high correlation between forecasts and  
observations can be surrounded by grid cells with similarly high correlation, or by grid cells with low correlation. In the  
former case, the grid cell is located in a region where the GCM forecasts tend to perform well. But in the latter case, the high  
correlation can be a suspicious outlier. Moreover, there exist clusters of grid cells with negative anomaly correlation, which  
means large (small) values of forecasts correspond to small (high) values of observations. In such a case, forecasts are  
70 cautiously wrong. Therefore, it is critical to characterize the different cases for spatial plotting and test whether the spatial  
patterns are significant and worth further attention.

In this paper, we are motivated to introduce spatial statistics [e.g., Di Luzio et al., 2008; Lu and Wong, 2008; Woldemeskel  
et al., 2013] to investigate the spatial plotting of anomaly correlation at the global scale. As will be shown later in this paper,  
the technique of spatial clustering facilitates the identification of significant patterns of high, neutral, and low anomaly  
75 correlation and provides an objective approach to interpreting the predictive performance of GCM forecasts. For the purpose  
of inter-comparison, the examination of significant patterns in spatial plotting has been conducted for ten sets of GCM  
seasonal precipitation forecasts in the North American Multi-Model Ensemble (NMME) experiment [Kirtman et al., 2014;  
Ma et al., 2016; Zhang et al., 2017]. In the remainder of the paper, the dataset of GCM seasonal forecasts is illustrated in  
Section 2; the spatial clustering using global and local Moran's  $I$  is detailed in Section 3; the results of anomaly correlation at  
80 the global scale and its clustering are shown in Section 4; the discussion and conclusions are respectively presented in  
Sections 5 and 6.

## 2 Data description

The NMME builds on existing GCMs in North America to provide quality-controlled forecast data to the community of  
climate research and applications. More than ten sets of GCM precipitation forecasts have been spatially regridded and  
85 temporally aggregated to form a consistent dataset [Kirtman et al., 2014]. Each set of forecasts overall has 5 dimensions.  
They are 1) start time  $s$ , when the forecasts are initialised; 2) lead time  $l$ , whose unit is month for the forecasts; 3) ensemble  
member  $n$ , which is meant to represent forecast uncertainty; 4) latitude  $y$ ; and 5) longitude  $x$ . Taking the precipitation  
forecasts of the Climate Forecast System version 2 [CFSv2, Saha et al., 2014] as an example,  $s$  is the beginning of each  
month and its value represents the number of months since January 1960;  $l$  is 0, 1, ..., 9, i.e., the forecasts are for month 0  
90 head (current month), month 1 ahead, ..., and month 9 ahead;  $n$  is numbered from 1 to 24, i.e., 24 ensemble members;  $y$  is  
from -90 to 90 while  $x$  is from 0 to 359, i.e., the spatial resolution is 1 degree by 1 degree (approximately 100 kilometres). In  
the meantime, NMME provides precipitation observations corresponding to the forecasts. Specifically, the Climate  
Prediction Center (CPC)'s merged analysis of precipitation [CMAP; Xie and Arkin, 1997; Xie et al., 2007], which is  
monthly, has been regridded to 1-degree resolution to verify GCM forecasts [Kirtman et al., 2014; Chen et al., 2017; Zhao et  
95 al., 2018].



**Table 1: Basic information on the ten sets of GCM forecasts from the NMME experiment**

Climate Centre	GCM	Number of ensemble members	Lead time (month)
Canadian Meteorological Center (CMC)	Canadian coupled model version 3 (CanCM3)	10	0–11
	Canadian coupled model version 4 (CanCM4)	10	0–11
Center for Ocean-Land-Atmosphere Studies, Rosenstiel School of Marine and Atmospheric Science (COLA-RSMAS)	Community climate system model version 3 (CCSM3)	6	0–11
	Community climate system model version 4 (CCSM4)	10	0–11
Geophysical Fluid Dynamics Laboratory (GFDL)	Climate model version 2.1 (CM2p1)	10	0–11
	Climate model version 2.1 (CM2p1-aer04)	10	0–11
	Climate model version 2.5 with forecast-oriented low ocean resolution (CM2p5-FLOR-A06)	12	0–11
	Climate model version 2.5 with forecast-oriented low ocean resolution (CM2p5-FLOR-B01)	12	0–11
National Center for Atmospheric Research (NCAR)	Community earth system model version 1 (CESM1)	10	0–11
National Centers for Environmental Prediction (NCEP)	Climate forecast system version 2 (CFSv2)	24	0–9

Ten sets of precipitation forecasts, as well as CMAP observations, in the NMME are downloaded from the International Research Institute at the Columbia University (<https://iridl.ldeo.columbia.edu/SOURCES/Models/NMME/>). Their retrospective forecasts are complete in the period from 1982 to 2010, and their real-time forecasts are updated by month since January 2010 [Merryfield et al., 2013; Saha et al., 2014; Jia et al., 2015]. Basic information on the forecasts are provided in Table 1. In the analysis, the attention is paid to the retrospective forecasts:

$$F_{GCM} = \left[ f_{s,l,n,y,x} \right]_{GCM} \quad (1)$$

In Eq. (1),  $f$  represents forecast values that are specified by the 5 dimensions;  $F$ , which is the set of forecasts, is marked by the GCM that generates the forecasts.

The observed precipitation corresponding to the forecasts is denoted as

$$O = \left[ o_{t,y,x} \right] \quad (t = s + l) \quad (2)$$

As shown in Eq. (2), the observation in total has three dimensions: time  $t$ , whose value is the addition of lead time  $l$  to start time  $s$  in the alignment of observation with forecast; latitude  $y$ ; and longitude  $x$ . It is pointed out that while  $F$  differs by GCM,  $O$  is the same across the ten sets of forecasts.

The anomaly correlation between  $F_{GCM}$  and  $O$  is obtained:



$$R_{GCM} = [r_{m,l,y,x}] \quad (3)$$

In which  $r$  and  $R$  are respectively the correlation coefficients and the set of correlation.  $R$ , which differs by GCM, has four dimensions: 1) a new dimension  $m$ , which is the month when the forecasts are generated, is created to substitute start time  $s$ . It is owing to that the calculation of anomaly correlation pools forecasts at multiple start times, e.g., January 1982, January 1983, ..., January 2010, since the performance of forecasts exhibits seasonality [Luo et al., 2014; Ma et al., 2016; Slater et al., 2017]; 2) lead time  $l$ ; 3) latitude  $y$ ; and 4) longitude  $x$ . Comparing Eq. (3) to Eq. (1), the dimension  $n$  of ensemble member is eliminated since the ensemble mean is taken in the calculation of anomaly correlation.

For selected GCM forecasts in month  $m$  and at lead time  $l$ , the anomaly correlation between ensemble mean and observation forms a two-dimensional array by latitude and longitude. Here, spatial plotting applies to the presentation of anomaly correlation at the global scale, and also at the regional scale. Following Eq. (3), the set of anomaly correlation is denoted as

$$R_{GCM,m,l} = [r_{y,x}] \quad (4)$$

In Eq. (4),  $y$  and  $x$  specify the location of grid cells. Denoting grid cell as  $i$ , the subscripts of latitude  $y$  and longitude  $x$  are merged into  $i$  for the purpose of simplicity

$$R_{GCM,m,l} = [r_i] \quad (5)$$

In which  $r_i$  represents the anomaly correlation at grid cell  $i$ , of which the latitude is  $y_i$  and the longitude is  $x_i$ .

### 3 Methods

The spatial plotting employs certain pre-selected colour schemes to represent the value of anomaly correlation and show the grid cell-wise anomaly correlation as it is [e.g., Yuan et al., 2011; Kirtman et al., 2014; Ma et al., 2016]. Spatial patterns that represent clusters of grid cells with high anomaly correlation are observed and highlighted in peer studies [e.g., Saha et al., 2014; Jia et al., 2015; Slater et al., 2017]. The spatial clustering associates anomaly correlation at neighbouring grid cells to one another and tests the significance of the patterns by random permutation. Following the standard formulations of spatial statistics [Anselin, 1995, 2006], the global Moran's  $I$  is calculated to examine the association among anomaly correlation at the global scale

$$I = \frac{\frac{1}{\sum_{i=1}^N \sum_{j=1, j \neq i}^N w_{i,j}} \sum_{i=1}^N \sum_{j=1, j \neq i}^N w_{i,j} (r_i - \bar{r})(r_j - \bar{r})}{\frac{1}{N} \sum_{i=1}^N (r_i - \bar{r})^2} \quad (6)$$



In which  $N$  is the number of grid cells indexed by  $i$  and  $j$  across the globe;  $\bar{r}$  is the mean value of anomaly correlation; and  $w_{i,j}$  is the spatial weighting coefficient that usually decays with the distance between  $i$  and  $j$  [Miller, 2004; Hao et al., 2016; Schmal et al., 2017]. At the right-hand side of Eq. (6), the denominator is the variance of  $r_i$  across all the grid cells; and the numerator is the spatially-weighted and -averaged covariance between  $r_i$  and  $r_j$ . Generally, the value of the global Moran's I ranges from -1 to 1. The similarity (dissimilarity) of  $r_i$  to the surrounding  $r_j$  makes  $I$  tend toward 1 (-1), while the random distribution of anomaly correlation makes  $I$  close to 0.

The spatial weight  $w_{i,j}$  plays an important part in the calculation of  $I$ . Following the inverse distance weighting (IDW) interpolation in geosciences [Di Luzio et al., 2008; Lu and Wong, 2008; Woldemeskel et al., 2013],  $w_{i,j}$  is formulated as follows

$$w_{i,j} = \frac{1}{d(i,j)^2} \quad (7)$$

In Eq. (6),  $d(i,j)$  is the Euclidean distance between grid cells  $i$  and  $j$ , i.e.,  $d(i,j) = \sqrt{(x_i - x_j)^2 + (y_i - y_j)^2}$ . In addition, the cut-off threshold for  $d(i,j)$  is set as 10 degrees (approximately 1,000 kilometres) to reduce the computational burden. That is,  $w_{i,j}$  is set as 0 if  $d(i,j)$  exceeds 10.

Adding to the global Moran's I, the local Moran's I is obtained to test whether  $r_i$  at a certain grid cell  $i$  significantly relates to surrounding  $r_j$  at the local scale [Anselin, 2006; Hao et al., 2016; Yuan et al., 2018]

$$I_i = \frac{(r_i - \bar{r}) \frac{\sum_{j=1, j \neq i}^N w_{i,j} (r_j - \bar{r})}{\sum_{j=1, j \neq i}^N w_{i,j}}}{\frac{1}{N} \sum_{i=1}^N (r_i - \bar{r})^2} \quad (8)$$

As shown in the above formulation,  $I_i$  is positive when  $r_i$  and the surrounding  $r_j$  are similarly high, or similarly low. On the other hand,  $I_i$  is negative when a high (low) value of  $r_i$  correspond to low (high) values of neighbouring  $r_j$ . Also,  $I_i$  can be close to zero when  $r_i$  or the surrounding  $r_j$  is close to the mean value. The significance of  $I_i$  is tested by random permutations. For each permutation, the values of  $r_j$  are randomly rearranged, and then the local Moran's I is re-calculated. The permutations obtained a reference distribution for  $I_i$  under the null hypothesis of randomly distributed anomaly correlation.

Given a significance level  $\alpha$ , the quantiles  $I_{\alpha/2}$  and  $I_{1-\alpha/2}$  are retrieved from the reference distribution. Therefore, the two-tailed test of  $I_i$  along with the anomaly correlation  $r_i$  facilitates spatial clustering and derives five cases:



$$case_i = \begin{cases} HH & (I_i > I_{1-\alpha/2}) \cup (r_i > \bar{r}) \\ HL & (I_i < I_{\alpha/2}) \cup (r_i > \bar{r}) \\ NS & (I_{\alpha/2} \leq I_i \leq I_{1-\alpha/2}) \\ LH & (I_i < I_{\alpha/2}) \cup (r_i < \bar{r}) \\ LL & (I_i > I_{1-\alpha/2}) \cup (r_i < \bar{r}) \end{cases} \quad (9)$$

As illustrated in Eq. (9), the first case HH, which is short for high-high, indicates that a high value of  $r_i$  is surrounded by high values of  $r_j$ ; the second case is HL, i.e., high-low – a high value of  $r_i$  surrounded by low values of  $r_j$ ; the third case is NS, i.e., not significant – the local association of  $r_i$  with surrounding  $r_j$  is not significant; the fourth case is LH, i.e., low-high – a low value of  $r_i$  surrounded by high values of  $r_j$ ; and the fifth case is LL, i.e., low-low – a low value of  $r_i$  surrounded by low values of  $r_j$ . In this way, the significance of patterns, which generally represent clusters of grid cells with high (low) anomaly correlation, is examined for spatial plotting of anomaly correlation.  $\alpha$  is set to be 0.05 in this paper.

## 4 Results

The spatial clustering is performed for the anomaly correlation of GCM seasonal precipitation forecasts. In the analysis, the attention is mainly concentrated on the forecasts of total precipitation in June, July, and August, which are generally boreal summer and Austral winter. The start time is June, and the forecasts at the lead times of 0, 1, and 2 months are aggregated to form the seasonal forecasts. In the meantime, forecasts initialized in September of total precipitation in September, October, and November, forecasts initialized in December of total precipitation in December, (the next) January, and (the next February), and forecasts initialized in March of total precipitation in March, April, and May are also investigated, with the results presented in the supplementary material.

### 4.1 Anomaly correlation of GCM forecasts

The anomaly correlation between ensemble mean and observation is evaluated for the ten sets of GCM precipitation forecasts in NMME. In Figure 1, the spatial plots employ a diverging red-blue colour scheme to represent the value of anomaly correlation. Red pixels indicate positive correlation, while blue pixels negative correlation. For each set of forecasts, many instances of red pixels can be observed. That is, forecasts exhibit promising performance with ensemble mean positively correlated with observation in many instances. Meanwhile, there also exist instances of blue pixels. In those instances, forecasts are generally not right because large (small) values of ensemble mean coincide with small (large) values of observation. While an inter-comparison of the ten sets of GCM forecasts in terms of anomaly correlation is presented in Figure 1, the anomaly correlation exhibits considerable spatial variability that hinders the analysis across the multiple sets of forecasts. As a result, it is none too easy to identify regions where the forecasts persistently exhibit promising predictive performance.



The first row of Figure 1 is for the forecasts generated by two Canadian GCMs. Although CanCM3 and CanCM4 share the ocean components and have slightly different atmospheric components [Merryfield et al., 2013], their anomaly correlation shows differences. For example, in Asia and Africa, the clusters of red pixels do not seem to overlap but differ instead; and  
180 in Australia, the anomaly correlation is high in Southeast and part of Western Australia for CanCM3 while it is high in East Australia for CanCM4. These results are in accordance with a previous finding that CanCM3 and CanCM4 tend to complement each other [Merryfield et al., 2013]. The second row of Figure 1 shows the performance of two sets of forecasts by COLA-RSMAS GCMs. Complementary performance is no longer seen. Instead, CCSM4 forecasts show higher anomaly correlation and largely outperform CCSM3 forecasts in North and South America, Africa, and Australia. The  
185 outperformance can be attributed to developments in ocean, atmospheric, and land components and new coupling infrastructure of CCSM4 [Gent et al., 2011].

The third and fourth rows of Figure 1 are for the forecasts produced by four GFDL GCMs. In the third row, CM2p1 and CM2p1-aer04 forecasts seem to exhibit similar anomaly correlation, which tends to be high in Northeast South America, Western Africa, and Southeast Australia. In the fourth row, CM2p5-FLOR-A06 and CM2p5-FLOR-B01 forecasts show  
190 similarly high anomaly correlation in Northeast and Southeast South America, Northeast Australia and part of West Australia. On the other hand, the anomaly correlation differs from the CM2p1 forecasts to the CM2p5-FLOR forecasts. Jia et al. [2015] illustrated that CM2p5-FLOR GCMs have higher-resolution atmospheric and land components but coarser-resolution ocean components than CM2p1 GCMs. It is likely modifications to the setting of GCMs that lead to the difference in predictive performance. The fifth row of Figure 1 is for NCAR-CESM1 and NCEP-CFSv2 forecasts. Compared to  
195 CESM1 forecasts, CFSv2 forecasts tend to exhibit similar anomaly correlation in South America and show higher anomaly correlation in Asia, Africa and Australia.



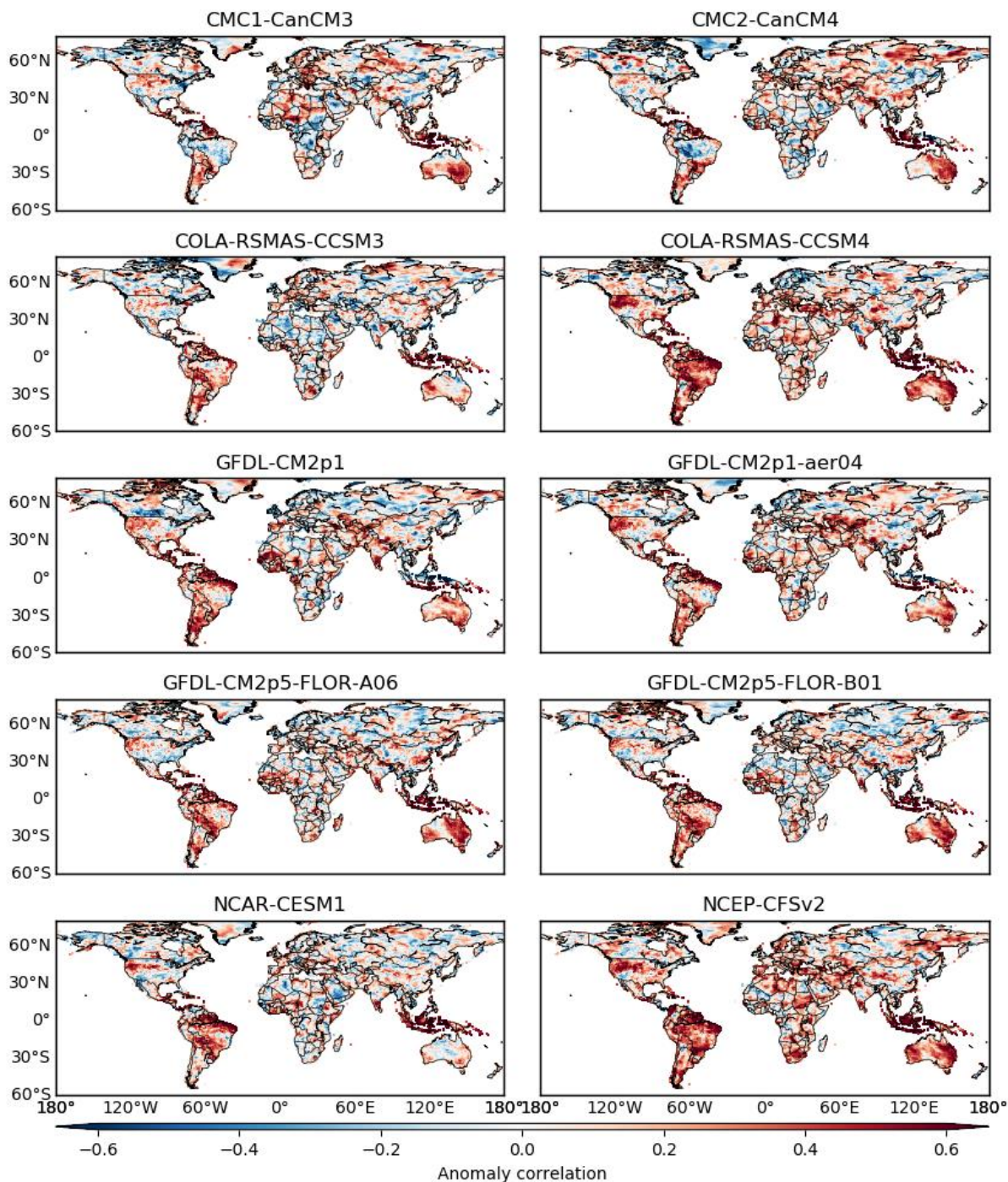


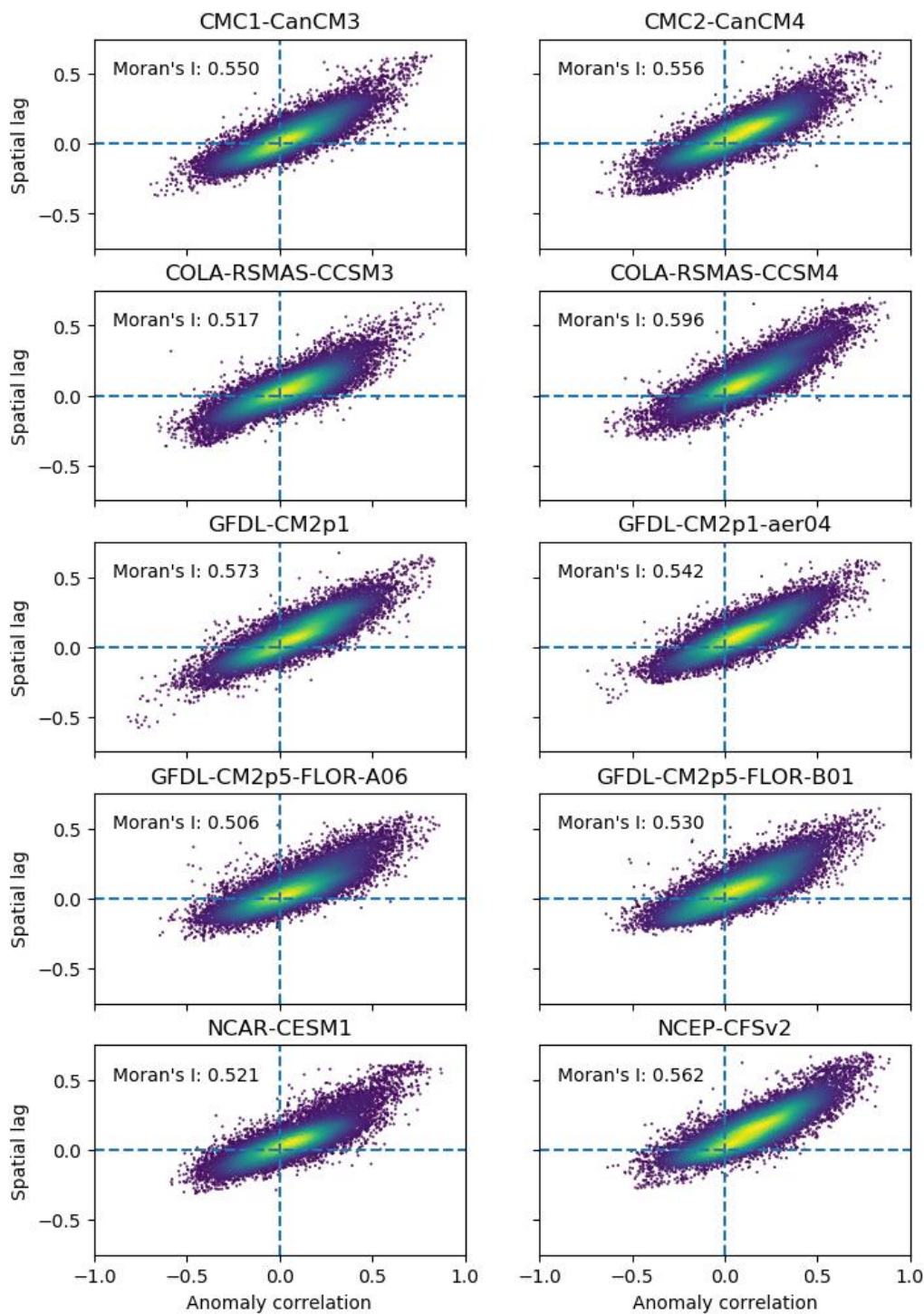
**Figure 1: Anomaly correlation between ensemble mean and observation for ten sets of GCM forecasts of seasonal precipitation. The forecasts are initialized in June and are for the total precipitation in June, July, and August**



#### 4.2 Anomaly correlation of GCM forecasts

In spatial analysis, one critical issue is how an attribute at one location relates to the attribute at neighbouring locations [Cliff and Ord, 1981; Anselin, 1995; Getis, 2007]. For anomaly correlation, the subplots of Figure 1 imply the existence of some relationships as there are clusters of red pixels and of blue pixels. As for the clusters, Figure 2 presents a thorough test of the relationships using the global Moran's I. Specifically, for all the grid cells across the globe, the anomaly correlation at each grid cell is plotted against the spatially-weighted and -averaged anomaly correlation, i.e., spatial lag [Miller, 2004; Hao et al., 2016; Schmal et al., 2017], at the surrounding grid cells.

Figure 2 uses a viridis heatmap to indicate the density of scatter points. It can be observed that the points frequently fall in the first quadrant under all the ten sets of forecasts. In accordance with clusters of red pixels in Figure 1, this result suggests that many grid cells are with positive anomaly correlation and that they tend to be surrounded by grid cells with positive anomaly correlation. Meanwhile, some points are in the third quadrant. It is due to that some grid cells are of negative anomaly correlation and are surrounded by grid cells with negative anomaly correlation. This outcome corresponds to the existence of clusters of blue grid cells in Figure 1. Also, there are points in the second and fourth quadrants. Overall, anomaly correlation at one grid cell positively relates to anomaly correlation at the neighbouring grid cells. The global Moran's I is above 0.500, with the p-value far smaller than 0.01, for all the ten sets of NMME seasonal forecasts. Adding to empirical findings from spatial plots, it is statistically verified that the spatial patterns implied by clusters of red (blue) pixels in Figure 1 are significant. That is, at the global scale, a grid cell with high (neutral, or low) anomaly correlation tends to be surrounded by grid cells with high (neutral, or low) anomaly correlation.



220 **Figure 2: Scatter plots of anomaly correlation at one grid cell against the corresponding spatial lag, i.e., spatially-weighted and -averaged anomaly correlation at surrounding grid cells**



### 4.3 Classification of grid cells by spatial analysis

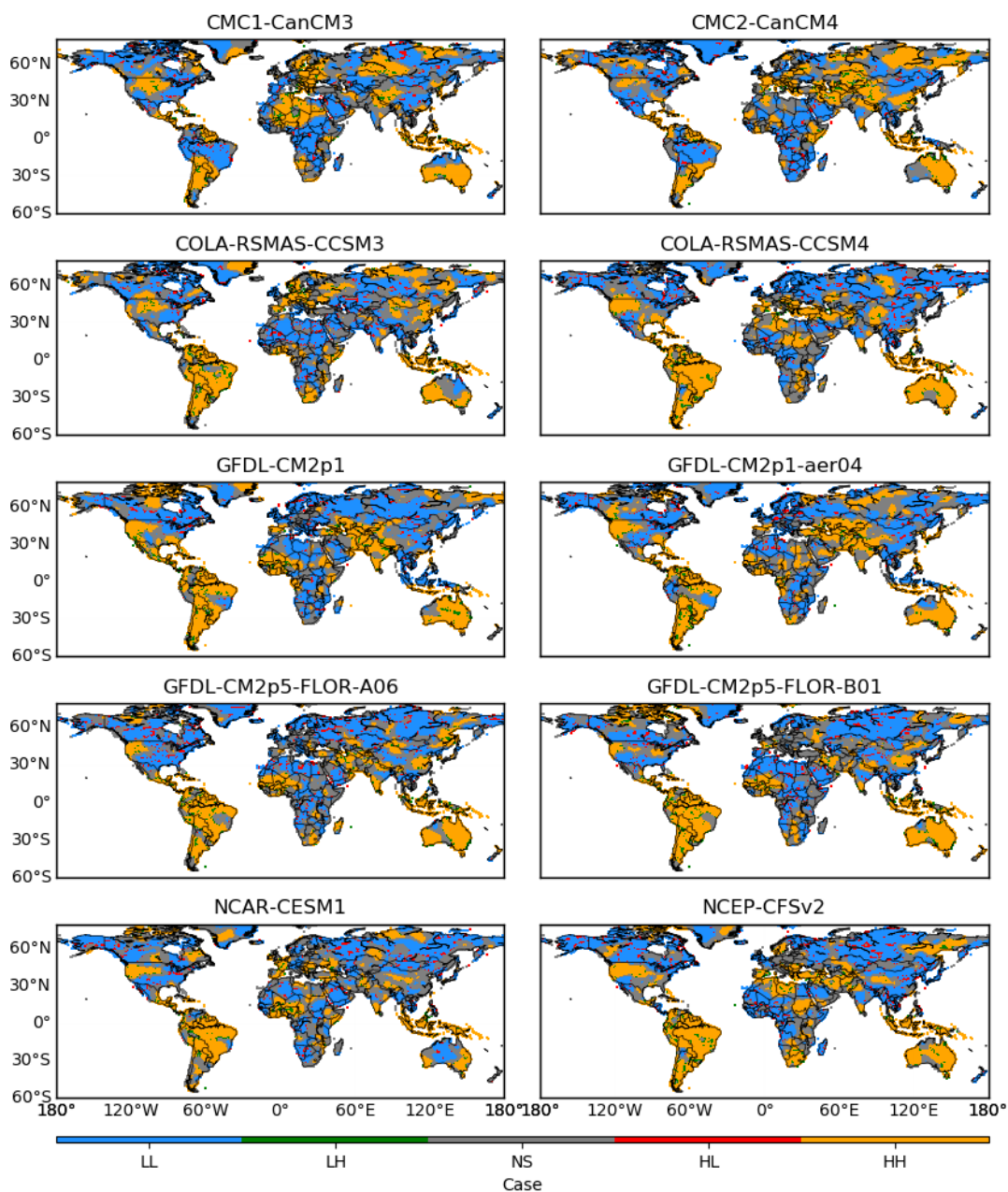
Furthermore, the local Moran's I classifies the grid cells across the globe into 5 cases under each of the ten sets of forecasts. In Figure 3, the five cases are marked by different colours. Specifically, the case HH is in orange, the case HL in red, the case NS in grey, the case LH in green, and the case LL in blue. A prominent finding is that the three cases of HH, NS, and LL have more instances than the other two cases of HL and LH. This result agrees to the spatial clustering of anomaly correlation in Figure 1 and to the distribution of scatter points in Figure 2. Comparing Figure 3 to Figure 1, it can be observed that orange regions generally correspond to clusters of red pixels, i.e., positive anomaly correlation, and that blue regions coincide with clusters of blue pixels, i.e., negative anomaly correlation. In the meantime, in-between orange and blue regions are grey regions. The implication is that regions with high and low anomaly correlation tend to be separated by regions with neutral anomaly correlation. While in Figure 1 the spatial variability of anomaly correlation complicates the analysis of predictive performance, the classification in Figure 3 facilitates a more effective inter-comparison of the ten sets of GCM forecasts.

The orange regions that correspond to clusters of grid cells with high anomaly correlation are of particular interest. Three findings are made from the spatial extent of orange regions. First of all, they tend to be similar under forecasts generated by the same climate center. For example, orange regions exist in a large part of South America for all the forecasts. Meanwhile, orange regions seem missing in the Amazon Basin under CMC1-CanCM3 and CMC2-CanCM4 forecasts while they tend to cover Amazon under COLA-RSMAS-CCSM3 and COLA-RSMAS-CCSM4 forecasts. The similarity versus difference can be owing to that GCMs developed at the same climate center tend to share components [Gent et al., 2011; Merryfield et al., 2013; Jia et al., 2015]. Secondly, orange regions seem to be affected by the setting of GCMs. There are four sets of forecasts by GFDL. In Western United States, orange regions are extensive under GFDL-CM2p1 and GFDL-CM2p1-aer04 forecasts but tend to be limited under GFDL-CM2p5-FLOR-A06 and GFDL-CM2p5-FLOR-B01 forecasts. This drastic difference can be due to the setting of FLOR, i.e., forecast-oriented low ocean resolution [Vecchi et al. 2014; Jia et al., 2015]. Thirdly, there are substantial regional variations possibly due to predictability of seasonal precipitation [Doblas-Reyes et al., 2013; Becker et al., 2014; Zhang et al., 2017]. For example, orange regions cover large part of Australia, in particular Southwest and Southeast Australia. However, they are not as extensive in Europe, Asia and Africa. It is possibly owing to that the climate in Australia is strongly affected by ENSO [Schepen et al., 2012; Hudson et al., 2017] and that the 10 GCMs in NMME tend to capture the effect of ENSO on June-July-August precipitation.

The blue regions correspond to clusters of grid cells with low anomaly correlation. They are generally indicative of locations where forecasts are not satisfactory. Under the ten sets of forecasts, blue regions can be observed in large parts of Europe, Asia, Africa, Canada, and Eastern United States. While orange regions show some relationships with the source and setting of GCMs, blue regions are more varying. In addition, they tend to be mixed with grey regions, which are indicative of



neutral anomaly correlation, and also with red and green regions. Overall, this outcome reflects the difficulty of climate  
255 forecasting at the global scale as there are complex land-ocean-atmosphere processes [Bauer et al., 2015; Kapnick et al.,  
2018; Kushnir et al., 2019]. It is noted that some red regions that represent the case HL are observed to be located inside blue  
regions. The implication is that some grid cells may happen to exhibit high anomaly correlation but their surrounding grid  
cells are of low anomaly correlation. From the perspective of spatial statistics, the high correlation is not trustworthy and can  
be regarded as outlier.



260

**Figure 3: Classification of grid cells across the globe into five cases using spatial clustering of anomaly correlation. The case HH is marked by orange, the case HL by red, the case NS by grey, the case LH by green, and the case LL by blue**

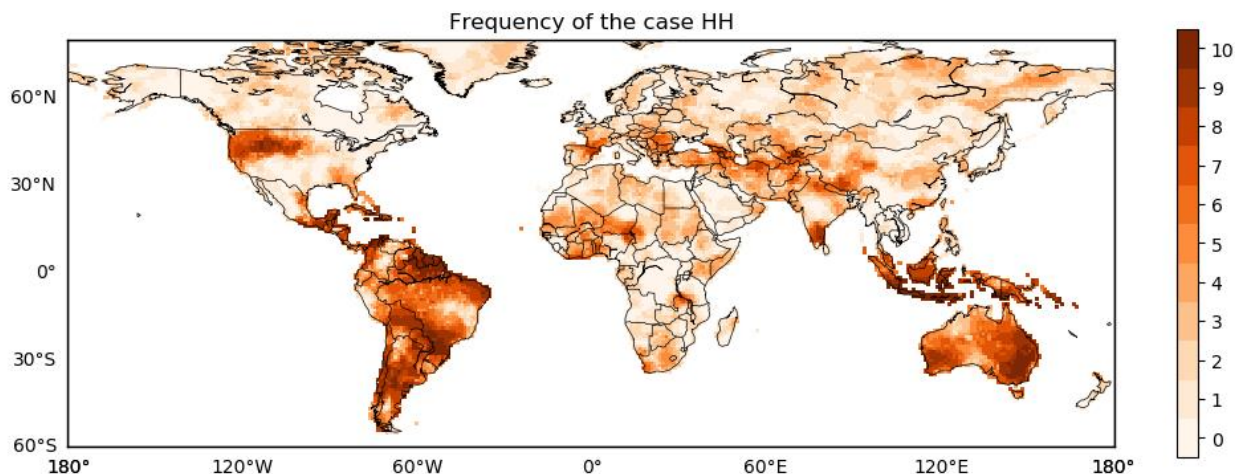


#### 265 4.4 Frequency of the case HH across the forecasts

While the orange regions of the case HH are indicative of promising predictive performance, grid cells classified under this case differ across the ten sets of forecasts. To handle the differences, the frequency that a grid cell falls into orange regions is counted for Figure 3. Figure 4 illustrates the frequency using a sequential colour scheme. For one grid cell, the frequency ranges from 0 to 10. That is, across the 10 sets of forecasts, one grid cell is with high anomaly correlation and is surrounded  
270 by grid cells with high anomaly correlation at the minimum for 0 times and at the maximum for 10 times.

Substantial regional variation is observed for the frequency of the case HH from Figure 4. In North America, the frequency is evidently higher in Western United States than in Eastern United States, Canada, and Mexico. Globally, the frequency is higher in South America than in Europe, Asia, and Africa. Also, the frequency is high in Australia and Southeast Asia. These results, which is a summary of orange regions in Figure 3, correspond to the spatial distribution of anomaly correlation in  
275 Figure 1. Mason and Goddard [2001] elaborated on the relationship between ENSO and global seasonal precipitation anomalies. For the total precipitation in June, July, and August, El Niño was shown to coincide with above-normal precipitation in parts of South and North America and below-normal precipitation in parts of Australia and Southeast Asia. By contrast, the impact of El Niño is not prominent for large parts of Europe, Asia, and Africa. From this perspective, it is speculated that the results in Figure 4 to some extent reflect the impact of ENSO at the global scale. Adding to previous  
280 findings that GCMs in NMME generate skilful forecasts of ENSO [e.g., Kirtman et al., 2014; Saha et al., 2014; Zhang et al., 2017], Figure 4 suggests that the GCMs also tend to capture ENSO-related precipitation.

Besides ENSO, there are other drivers of global climate. For example, North Atlantic Oscillation (NAO) and Arctic Oscillation (AO) extensively affect the climate in Europe, Asia, and North America [Hurrell et al., 2001; Ambaum et al., 2002]. Several sea surface temperature indices of the Atlantic and Indian Oceans and ENSO jointly impact the climate in  
285 Africa [Rowell, 2013]. According to Figure 4, there are still substantial rooms for improvements of seasonal precipitation forecasts in June, July, and August for large parts of Europe, Asia, and Africa. It is possibly because GCM formulations of other climate indices are not as effective as the formulations of ENSO. In the meantime, the difficulty of global climate forecasting due to spatially-temporally varying teleconnections between regional precipitation and global climate drivers is noted [Merryfield et al., 2013; Saha et al., 2014; Jia et al., 2015; Hudson et al., 2017; Kushnir et al., 2019].



290

**Figure 4: The number of the case HH across the ten sets of NMME seasonal forecasts at the global cells**

#### 4.5 Distribution of the frequency of the case HH

The percentage and cumulative percentage of the frequency of the case HH are shown by bar and line plots in Figure 5, respectively. The frequency of 0 corresponds to a percentage of nearly 20%. This outcome means that about 20% of the grid cells across the globe do not fall into the case HH under any of the ten sets of forecasts. Another interpretation of this result is that about 80% of the grid cells fall into the case HH under at least one of the ten sets of forecasts. This result is in contrast to Figure 3 suggesting that orange regions are limited under each of the ten set of forecasts. It highlights the spatial complementarity among the multiple sets of GCM forecasts [Doblas-Reyes et al., 2013; Merryfield et al., 2013; Jia et al., 2015]. In the meantime, the percentages corresponding to the frequencies of 5, 6, ..., 10 are all below 5% and the cumulative percentage reaches 80% at the frequency of 4. This result reflects that the performances of the different sets of forecasts are not the same. Instead, they tend to differ from one another. In other words, for certain regions, some sets of GCM forecasts may not be satisfactory while some other sets of GCM forecasts may be promising. Generally, the results in Figure 5 suggest the complementarity among the GCM forecasts in NMME and call for the use of model averaging methods to assign spatially-varying weighting coefficients and take advantage of the multiple sets of forecasts [Wang et al., 2012; Becker et al., 2014; Kirtman et al., 2014].

305



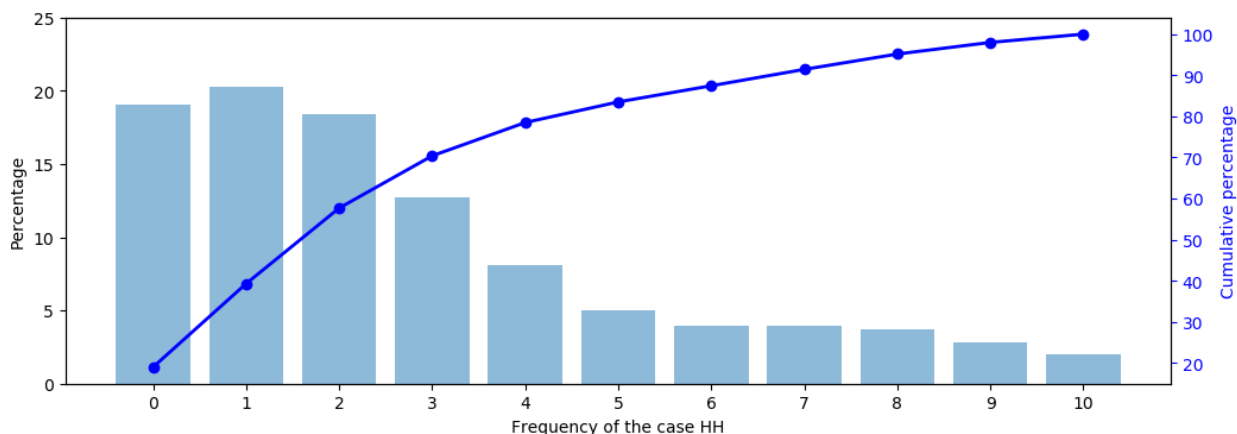


**Figure 5: Percentage (bar plot) and cumulative percentage (line plot) of the number of the case HH**

310

## 5 Discussion

We have identified significant spatial patterns [Anselin, 1995; Miller, 2004; Schmal et al., 2017] from spatial plots of anomaly correlation, which have been widely used to illustrate the predictive performance of GCM forecasts. The test of significance is conducted by global and local Moran's I for ten sets of forecasts in NMME. The global Moran's I indicates that at the global scale anomaly correlation at one grid cell significantly relates to anomaly correlation at neighbouring grid cells, while the local Moran's I reveals clusters of grid cells with high anomaly correlation. Across the ten sets of forecasts, the clusters tend to be persistently observed in the Western United States, South America, Australia, and Southeast Asia, possibly due to the fact that the GCMs tend to capture the ENSO-related precipitation. Besides the seasonal forecasts for June, July, and August, the spatial clustering has also been applied to forecasts for September, October, and November, forecasts for December, January, and, and forecasts for March, April, and May. The results, which are illustrated in the supplementary material, are in accordance with Figures 1 to 5 and indicate the existence of significant patterns. Meanwhile, the spatial extents of clusters vary by season. The variability can be due to that the predictability of precipitation varies by season and that the effectiveness of GCMs also differs by season [Doblas-Reyes et al., 2013; Becker et al., 2014; Yuan et al., 2015; Hudson et al., 2017; Kushnir et al., 2019]. Nevertheless, the spatial clustering yields insights into the predictive performance and can serve as an effective approach to the inter-comparison of GCM forecasts.

The spatial clustering ties anomaly correlation at neighbouring grid cells to one another and converts the continuous anomaly correlation into five categorical cases. Similar to the technique of moving average in time-series analysis, the categorical cases serve as a filter to reduce noise for the identification of spatial patterns. They handle the spatial variability of anomaly correlation and facilitate analysis across different sets of forecasts. The forecasts produced by the same climate center tend to



330 exhibit similar predictive performance and the setting of GCMs leads to different predictive performance. These findings are  
obtained through ten sets of forecasts in NMME. Given the fact that the global and local Moran's I are flexible and easy to  
compute, they are ready to be extended in future analysis to other sets of forecasts, such as forecasts generated by Systems 4  
and 5 at the European Centre for Medium-Range Weather Forecasts (ECMWF) and by other GCMs in Europe and Asia  
[Alfieri et al., 2013; Bellprat et al., 2019; Kushnir et al., 2019]. A more extensive inter-comparison would contribute to better  
335 understanding of the predictive performance and illustrate the advantages of different sets of GCM forecasts. Of particular  
interest is to explore which GCMs achieve promising predictive performance in large parts of Europe, Asia, and Africa. In  
the meantime, it is meaningful to account for the dynamics of global climate and investigate the model physics that leads to  
the improved performance.

The spatial clustering is a popular approach to geographical, ecological, and environmental modelling [e.g., Anselin, 1995,  
340 2006; Miller, 2004; Hao et al., 2016; Schmal et al., 2017]. Meanwhile, its use appears to be uncommon in the forecasting  
area. A possible cause is that the objective of forecasting is usually location-specific. In other words, forecasts are produced  
for a certain site/watershed and then verified using the corresponding observations, of which the process does not involve  
other sites/watersheds. In this paper, the analysis of GCM forecasts in NMME reveals that forecasts at neighbouring  
locations positively relate to one another. The indication is that the skill at one location can to some extent be inferred from  
345 adjacent locations. This result facilitates a new perspective for the verification of GCM forecasts. If a grid cell with high  
anomaly correlation is surrounded by grid cells with high anomaly correlation, the promising predictive performance at that  
grid cell can be confirmed. However, if the surrounding grid cells are with low, or even negative, anomaly correlation, then  
the high anomaly correlation is identified to be suspicious outlier. Under that circumstance, further examination of the  
predictive performance is highly demanded to avoid undue optimism.

## 350 **6 Conclusions**

Fully-coupled GCMs perform physically-based forecasting of the global climate and generate a vast amount of spatial-  
temporal forecast data. The predictive performance is of both societal and scientific importance in the applications of these  
GCM forecasts. Focusing on the anomaly correlation between forecast ensemble mean and observation, we have conducted  
in-depth spatial analysis for ten sets of forecasts in NMME and identified significant patterns from the spatial plotting of  
355 anomaly correlation. In the analysis of spatial clustering, grid cells across the globe are classified into five categories – HH,  
HL, NS, LH, and LL – depending on the anomaly correlation at that grid cell and the surrounding grid cells. The regions of  
grid cells with high, neutral, and low anomaly correlation are effectively identified. Further, effective inter-comparison  
across multiple sets of GCM forecasts is facilitated. While the analysis is concentrated on the spatial plotting of anomaly  
correlation, the framework readily applies to other metrics of GCM forecasts, such as bias, reliability, and skill. Moreover,  
360 the framework can be extended to GCM forecasts of other climate variables, for example precipitation and wind speed,  
serving as a tool to explore GCM forecasts and interpret the predictive performance.



## Acknowledgements

The work is supported by the Natural Science Foundation of China, the Guangdong Provincial Department of Science and Technology, and the Ministry of Science and Technology of China.

## 365 Data availability

Both the observations and the forecasts can be downloaded from the International Research Institute for Climate and Society, Earth Institute, Columbia University (<https://iridl.ldeo.columbia.edu/SOURCES/Models/NMME/>)

## Competing interests

The authors declare that they have no conflict of interest.

## 370 Author contributions

TZ, WZ, and YZ designed the experiment and performed the data analysis. TZ and XC collected the data. TZ prepared the manuscript with contributions from all co-authors.

## References

- Alfieri, L., Burek, P., Dutra, E., Krzeminski, B., Muraro, D., Thielen, J., and Pappenberger, F.: GloFAS - global ensemble streamflow forecasting and flood early warning, *Hydrology and Earth System Sciences*, 17, 1161-1175, <https://doi.org/10.5194/hess-17-1161-2013>, 2013.
- Ambaum, M. H. P., Hoskins, B. J., and Stephenson, D. B.: Arctic oscillation or North Atlantic oscillation? (vol 14, pg 3495, 2001), *Journal of Climate*, 15, 553-553, [https://doi.org/10.1175/1520-0442\(2002\)015<0553:c>2.0.co;2](https://doi.org/10.1175/1520-0442(2002)015<0553:c>2.0.co;2), 2002.
- Anselin, L.: LOCAL INDICATORS OF SPATIAL ASSOCIATION - LISA, *Geographical Analysis*, 27, 93-115, <https://doi.org/10.1111/j.1538-4632.1995.tb00338.x>, 1995.
- Anselin, L., Syabri, I., and Kho, Y.: GeoDa: An introduction to spatial data analysis, *Geographical Analysis*, 38, 5-22, <https://doi.org/10.1111/j.0016-7363.2005.00671.x>, 2006.
- Bauer, P., Thorpe, A., and Brunet, G.: The quiet revolution of numerical weather prediction, *Nature*, 525, 47-55, <https://doi.org/10.1038/nature14956>, 2015.
- 385 Becker, E., van den Dool, H., and Zhang, Q.: Predictability and Forecast Skill in NMME, *Journal of Climate*, 27, 5891-5906, <https://doi.org/10.1175/jcli-d-13-00597.1>, 2014.



- Bellprat, O., Guemas, V., Doblas-Reyes, F., and Donat, M. G.: Towards reliable extreme weather and climate event attribution, *Nature Communications*, 10, <https://doi.org/10.1038/s41467-019-09729-2>, 2019.
- Chen, L.-C., Van den Dool, H., Becker, E., and Zhang, Q.: ENSO Precipitation and Temperature Forecasts in the North  
390 American Multimodel Ensemble: Composite Analysis and Validation, *Journal of Climate*, 30, 1103-1125,  
<https://doi.org/10.1175/jcli-d-15-0903.1>, 2017.
- Cliff, A. D., and Ord, J. K.: *Spatial processes: models & applications*, Taylor & Francis, <https://doi.org/10.1086/412797>,  
1981.
- Crochemore, L., Ramos, M. H., and Pappenberger, F.: Bias correcting precipitation forecasts to improve the skill of seasonal  
395 streamflow forecasts, *Hydrology and Earth System Sciences*, 20, 3601-3618, <https://doi.org/10.5194/hess-20-3601-2016>,  
2016.
- Di Luzio, M., Johnson, G. L., Daly, C., Eischeid, J. K., and Arnold, J. G.: Constructing retrospective gridded daily  
precipitation and temperature datasets for the conterminous United States, *Journal of Applied Meteorology and Climatology*,  
47, 475-497, <https://doi.org/10.1175/2007jamc1356.1>, 2008.
- 400 Doblas-Reyes, F. J., Garcia-Serrano, J., Lienert, F., Biescas, A. P., and Rodrigues, L. R. L.: Seasonal climate predictability  
and forecasting: status and prospects, *Wiley Interdisciplinary Reviews-Climate Change*, 4, 245-268,  
<https://doi.org/10.1002/wcc.217>, 2013.
- Gent, P. R., Danabasoglu, G., Donner, L. J., Holland, M. M., Hunke, E. C., Jayne, S. R., Lawrence, D. M., Neale, R. B.,  
Rasch, P. J., Vertenstein, M., Worley, P. H., Yang, Z. L., and Zhang, M. H.: The Community Climate System Model Version  
405 4, *Journal of Climate*, 24, 4973-4991, <https://doi.org/10.1175/2011jcli4083.1>, 2011.
- Getis, A.: Reflections on spatial autocorrelation, *Regional Science and Urban Economics*, 37, 491-496,  
<https://doi.org/10.1016/j.regsciurbeco.2007.04.005>, 2007.
- Gneiting, T., Balabdaoui, F., and Raftery, A. E.: Probabilistic forecasts, calibration and sharpness, *Journal of the Royal  
Statistical Society Series B-Statistical Methodology*, 69, 243-268, <https://doi.org/10.1111/j.1467-9868.2007.00587.x>, 2007.
- 410 Hao, Y., Liu, Y. M., Weng, J. H., and Gao, Y. X.: Does the Environmental Kuznets Curve for coal consumption in China  
exist? New evidence from spatial econometric analysis, *Energy*, 114, 1214-1223,  
<https://doi.org/10.1016/j.energy.2016.08.075>, 2016.
- Hersbach, H.: Decomposition of the continuous ranked probability score for ensemble prediction systems, *Weather and  
Forecasting*, 15, 559-570, [https://doi.org/10.1175/1520-0434\(2000\)015<0559:dotcrp>2.0.co;2](https://doi.org/10.1175/1520-0434(2000)015<0559:dotcrp>2.0.co;2), 2000.
- 415 Hudson, D., Alves, O., Hendon, H. H., Lim, E.-P., Liu, G., Luo, J.-J., MacLachlan, C., Marshall, A. G., Shi, L., Wang, G.,  
Wedd, R., Young, G., Zhao, M., and Zhou, X.: ACCESS-S1: The new Bureau of Meteorology multi-week to seasonal  
prediction system, *Journal of Southern Hemisphere Earth Systems Science*, 67, 132-159, 10.22499/3.6703.001, 2017.
- Hurrell, J. W., Kushnir, Y., and Visbeck, M.: Climate - The North Atlantic oscillation, *Science*, 291, 603-605,  
<https://doi.org/10.1126/science.1058761>, 2001.



- 420 Jia, L. W., Yang, X. S., Vecchi, G. A., Gudgel, R. G., Delworth, T. L., Rosati, A., Stern, W. F., Wittenberg, A. T., Krishnamurthy, L., Zhang, S. Q., Msadek, R., Kapnick, S., Underwood, S., Zeng, F. R., Anderson, W. G., Balaji, V., and Dixon, K.: Improved Seasonal Prediction of Temperature and Precipitation over Land in a High-Resolution GFDL Climate Model, *Journal of Climate*, 28, 2044-2062, <https://doi.org/10.1175/jcli-d-14-00112.1>, 2015.
- Kirtman, B. P., Min, D., Infanti, J. M., Kinter, J. L., Paolino, D. A., Zhang, Q., van den Dool, H., Saha, S., Mendez, M. P.,  
425 Becker, E., Peng, P. T., Tripp, P., Huang, J., DeWitt, D. G., Tippett, M. K., Barnston, A. G., Li, S. H., Rosati, A., Schubert, S. D., Rienecker, M., Suarez, M., Li, Z. E., Marshak, J., Lim, Y. K., Tribbia, J., Pegion, K., Merryfield, W. J., Denis, B., and Wood, E. F.: THE NORTH AMERICAN MULTIMODEL ENSEMBLE Phase-1 Seasonal-to-Interannual Prediction; Phase-2 toward Developing Intraseasonal Prediction, *Bulletin of the American Meteorological Society*, 95, 585-601, <https://doi.org/10.1175/bams-d-12-00050.1>, 2014.
- 430 Kushnir, Y., Scaife, A. A., Arritt, R., Balsamo, G., Boer, G., Doblas-Reyes, F., Hawkins, E., Kimoto, M., Kolli, R. K., Kumar, A., Matei, D., Matthes, K., Muller, W. A., O'Kane, T., Perlwitz, J., Power, S., Raphael, M., Shimpo, A., Smith, D., Tuma, M., and Wu, B.: Towards operational predictions of the near-term climate, *Nature Climate Change*, 9, 94-101, <https://doi.org/10.1038/s41558-018-0359-7>, 2019.
- Lu, G. Y., and Wong, D. W.: An adaptive inverse-distance weighting spatial interpolation technique, *Computers &*  
435 *Geosciences*, 34, 1044-1055, <https://doi.org/10.1016/j.cageo.2007.07.010>, 2008.
- Luo, L., Tang, W., Lin, Z., and Wood, E. F.: Evaluation of summer temperature and precipitation predictions from NCEP CFSv2 retrospective forecast over China, *Climate Dynamics*, 41, 2213-2230, <https://doi.org/10.1007/s00382-013-1927-1>, 2013.
- Ma, F., Ye, A., Deng, X., Zhou, Z., Liu, X., Duan, Q., Xu, J., Miao, C., Di, Z., and Gong, W.: Evaluating the skill of NMME  
440 seasonal precipitation ensemble predictions for 17 hydroclimatic regions in continental China, *International Journal of Climatology*, 36, 132-144, <https://doi.org/10.1002/joc.4333>, 2016.
- Mason, S. J., and Goddard, L.: Probabilistic precipitation anomalies associated with ENSO, *Bulletin of the American Meteorological Society*, 82, 619-638, [https://doi.org/10.1175/1520-0477\(2001\)082<0619:ppaawe>2.3.co;2](https://doi.org/10.1175/1520-0477(2001)082<0619:ppaawe>2.3.co;2), 2001.
- Merryfield, W. J., Lee, W. S., Boer, G. J., Kharin, V. V., Scinocca, J. F., Flato, G. M., Ajayamohan, R. S., Fyfe, J. C., Tang,  
445 Y. M., and Polavarapu, S.: The Canadian Seasonal to Interannual Prediction System. Part I: Models and Initialization, *Monthly Weather Review*, 141, 2910-2945, <https://doi.org/10.1175/mwr-d-12-00216.1>, 2013.
- Miller, H. J.: Tobler's First Law and spatial analysis, *Annals of the Association of American Geographers*, 94, 284-289, <https://doi.org/10.1111/j.1467-8306.2004.09402005.x>, 2004.
- Murphy, A. H.: What is a good forecast? An essay on the nature of goodness in weather forecasting, *Weather and forecasting*,  
450 8, 281-293, [https://doi.org/10.1175/1520-0434\(1993\)008<0281:WIAGFA>2.0.CO;2](https://doi.org/10.1175/1520-0434(1993)008<0281:WIAGFA>2.0.CO;2), 1993.
- Pappenberger, F., Cloke, H. L., and Baugh, C. A.: Cartograms for Use in Forecasting Weather-Driven Natural Hazards, *Cartographic Journal*, 56, 134-145, <https://doi.org/10.1080/00087041.2018.1534358>, 2019.



- Rowell, D. P.: Simulating SST Teleconnections to Africa: What is the State of the Art?, *Journal of Climate*, 26, 5397-5418, <https://doi.org/10.1175/jcli-d-12-00761.1>, 2013.
- 455 Saha, S., Moorthi, S., Wu, X. R., Wang, J., Nadiga, S., Tripp, P., Behringer, D., Hou, Y. T., Chuang, H. Y., Iredell, M., Ek, M., Meng, J., Yang, R. Q., Mendez, M. P., Van Den Dool, H., Zhang, Q., Wang, W. Q., Chen, M. Y., and Becker, E.: The NCEP Climate Forecast System Version 2, *Journal of Climate*, 27, 2185-2208, <https://doi.org/10.1175/jcli-d-12-00823.1>, 2014.
- Schepen, A., Wang, Q. J., and Robertson, D.: Evidence for Using Lagged Climate Indices to Forecast Australian Seasonal  
460 Rainfall, *Journal of Climate*, 25, 1230-1246, <https://doi.org/10.1175/jcli-d-11-00156.1>, 2012.
- Schmal, C., Myung, J., Herzel, H., and Bordyugov, G.: Moran's I quantifies spatio-temporal pattern formation in neural imaging data, *Bioinformatics*, 33, 3072-3079, <https://doi.org/10.1093/bioinformatics/btx351>, 2017.
- Sheffield, J., Wood, E. F., Chaney, N., Guan, K. Y., Sadri, S., Yuan, X., Olang, L., Abou, A., Ali, A., Demuth, S., and Ogallo, L.: A DROUGHT MONITORING AND FORECASTING SYSTEM FOR SUB-SAHARA AFRICAN WATER  
465 RESOURCES AND FOOD SECURITY, *Bulletin of the American Meteorological Society*, 95, 861-+, <https://doi.org/10.1175/bams-d-12-00124.1>, 2014.
- Slater, L. J., Villarini, G., and Bradley, A. A.: Weighting of NMME temperature and precipitation forecasts across Europe, *Journal of Hydrology*, 552, 646-659, <https://doi.org/10.1016/j.jhydrol.2017.07.029>, 2017.
- Tian, D., Wood, E. F., and Yuan, X.: CFSv2-based sub-seasonal precipitation and temperature forecast skill over the  
470 contiguous United States, *Hydrology and Earth System Sciences*, 21, 1477-1490, <https://doi.org/10.5194/hess-21-1477-2017>, 2017.
- Tobler, W. R.: A computer movie simulating urban growth in the Detroit region, *Economic geography*, 46, 234-240, 1970.
- Vecchi, G. A., Delworth, T., Gudgel, R., Kapnick, S., Rosati, A., Wittenberg, A. T., Zeng, F., Anderson, W., Balaji, V., Dixon, K., Jia, L., Kim, H. S., Krishnamurthy, L., Msadek, R., Stern, W. F., Underwood, S. D., Villarini, G., Yang, X., and  
475 Zhang, S.: On the Seasonal Forecasting of Regional Tropical Cyclone Activity, *Journal of Climate*, 27, 7994-8016, <https://doi.org/10.1175/jcli-d-14-00158.1>, 2014.
- Wang, Q. J., Schepen, A., and Robertson, D. E.: Merging Seasonal Rainfall Forecasts from Multiple Statistical Models through Bayesian Model Averaging, *Journal of Climate*, 25, 5524-5537, <https://doi.org/10.1175/jcli-d-11-00386.1>, 2012.
- Woldemeskel, F. M., Sivakumar, B., and Sharma, A.: Merging gauge and satellite rainfall with specification of associated  
480 uncertainty across Australia, *Journal of Hydrology*, 499, 167-176, <https://doi.org/10.1016/j.jhydrol.2013.06.039>, 2013.
- Wu, Z., Wang, B., Li, J., and Jin, F.-F.: An empirical seasonal prediction model of the east Asian summer monsoon using ENSO and NAO, *Journal of Geophysical Research-Atmospheres*, 114, <https://doi.org/10.1029/2009jd011733>, 2009.
- Xie, P., and Arkin, P. A.: Global Precipitation: A 17-Year Monthly Analysis Based on Gauge Observations, Satellite Estimates, and Numerical Model Outputs, *Bulletin of the American Meteorological Society*, 78, 2539-2558,  
485 [https://doi.org/10.1175/1520-0477\(1997\)078<2539:gpayma>2.0.co;2](https://doi.org/10.1175/1520-0477(1997)078<2539:gpayma>2.0.co;2), 1997.



- Xie, P., Arkin, P. A., and Janowiak, J. E.: CMAP: The CPC merged analysis of precipitation, in: Measuring precipitation from space, Springer, 319-328, <https://doi.org/10.1007/978-1-4020-5835-6>, 2007.
- Yuan, X., Wood, E. F., Luo, L., and Pan, M.: A first look at Climate Forecast System version 2 (CFSv2) for hydrological seasonal prediction, *Geophysical research letters*, 38, <https://doi.org/10.1029/2011GL047792>, 2011.
- 490 Yuan, X., Wood, E. F., Roundy, J. K., and Pan, M.: CFSv2-based seasonal hydroclimatic forecasts over the conterminous United States, *Journal of Climate*, 26, 4828-4847, <https://doi.org/10.1175/JCLI-D-12-00683.1>, 2013.
- Yuan, X., Wood, E. F., and Ma, Z.: A review on climate-model-based seasonal hydrologic forecasting: physical understanding and system development, *Wiley Interdisciplinary Reviews: Water*, 2, 523-536, <https://doi.org/10.1002/wat2.1088>, 2015.
- 495 Yuan, Y. M., Cave, M., and Zhang, C. S.: Using Local Moran's I to identify contamination hotspots of rare earth elements in urban soils of London, *Applied Geochemistry*, 88, 167-178, <https://doi.org/10.1016/j.apgeochem.2017.07.011>, 2018.
- Zhang, W., Villarini, G., Slater, L., Vecchi, G. A., and Bradley, A. A.: Improved ENSO Forecasting Using Bayesian Updating and the North American Multimodel Ensemble (NMME), *Journal of Climate*, 30, 9007-9025, <https://doi.org/10.1175/jcli-d-17-0073.1>, 2017.
- 500 Zhao, T. T. G., Bennett, J. C., Wang, Q. J., Schepen, A., Wood, A. W., Robertson, D. E., and Ramos, M. H.: How Suitable is Quantile Mapping For Postprocessing GCM Precipitation Forecasts?, *Journal of Climate*, 30, 3185-3196, <https://doi.org/10.1175/jcli-d-16-0652.1>, 2017.
- Zhao, T. T. G., Chen, X. H., Liu, P., Zhang, Y. Y., Liu, B. J., and Lin, K. R.: Relating Anomaly Correlation to Lead Time: Principal Component Analysis of NMME Forecasts of Summer Precipitation in China, *Journal of Geophysical Research-*
- 505 *Atmospheres*, 123, 6039-6052, <https://doi.org/10.1029/2018jd028267>, 2018.
- Zhao, T. T. G., Wang, Q. J., Schepen, A., and Griffiths, M.: Ensemble forecasting of monthly and seasonal reference crop evapotranspiration based on global climate model outputs, *Agricultural and Forest Meteorology*, 264, 114-124, <https://doi.org/10.1016/j.agrformet.2018.10.001>, 2019.